IEEE Access
Multidisciplinary | Rapid Review | Open Access Journal

Received May 25, 2022, accepted June 6, 2022, date of publication June 13, 2022, date of current version June 16, 2022.

Digital Object Identifier 10.1109/ACCESS.2022.3182478

Shape Reconstruction of Concave Objects Based on High-Order Boundary Scattering Transform for Millimeter-Wave Near-Field Imaging

JUNHUI YANG, XIAODONG ZHUGE, AND HUI QIAO
School of Electronics and Information Engineering, Beihang University, Beijing 100191, China
Corresponding author: Xiaodong Zhuge (zhuge@buaa.edu.cn)

This work was supported by the National Natural Science Foundation of China under Grant 62171011.

ABSTRACT Millimeter-wave near-field imaging provides a promising solution for potential sensing applications. Although in many cases only the shape of the object is required, the conventional method often carries out a full image reconstruction of the target, thus suffers from slow imaging speed and high computational complexity. Moreover, conventional imaging results exhibit severe artifacts when facing complex concave targets due to high-order scattering. Both problems pose a significant obstacle for achieving sufficient accuracy in target recognition. To address these issues, this paper proposes a new shape reconstruction technique for millimeter-wave imaging of complex concave objects based on a high-order boundary scattering transform (HBST). Target contours are directly obtained by establishing a transform formula between the received wavefront under multiple reflections and the target boundaries. Multiple reflections propagation omitted in conventional imaging are fully included in the derivation of the HBST. Numerical simulations and experimental results are presented to verify the applicability and effectiveness of the proposed technique for dihedral-like structures.

INDEX TERMS Concave structure, boundary scattering transform, higher-order artifacts, multiple reflections, shape reconstruction.

I. INTRODUCTION

Millimeter waves have longer wavelength compared to light waves and can easily penetrate many optically opaque objects, such as ordinary clothing materials, dense vegetation, smoke, fog, walls, etc. Therefore, millimeter waves are commonly used in through walls imaging, security screening, ground-penetrating radar, etc.

High quality image reconstruction algorithms are required in order to obtain an accurate image of the target. A series of millimeter-wave active imaging algorithms have been proposed for target detection and identification. The back-projection (BP) [1]–[3], a classical time-domain algorithm, is one of the most commonly used technique, but suffers from intensive computation and low efficiency. Some algorithms based on the field of synthetic aperture imaging (SAR) have also been presented. The wave-number domain (ω-k) algorithm [4], [5] requires Stolt interpolation in the two-dimensional frequency domain, which could affects the image quality. Range-Doppler (RD) algorithm [6], [7] also requires interpolation to eliminate longitudinal and lateral inter-coupling caused by range migration. Chirp scaling (CS) algorithm [8], [9] avoids interpolation operation, but the range spectrum of echo signal will shift in this algorithm. Based on those traditional imaging algorithms, some human imaging applications such as SafeView and QPS [10]–[12] have also achieved promising results in detecting concealed contraband in the human body. However, they usually encounter problems such as large arrays, high computational effort and slow imaging speed. Meanwhile, the ultimate goal of contraband detection is not to image the target, but to detect, extract contours and eventually identify the hidden contraband.

It is possible to recover the contour of the target directly from the received wavefront without a full image reconstruction process by directly establishing the relationship between the received wavefront and the target shape with a boundary scattering transform (BST) [13]. The high-speed 3-D imaging algorithm, a shape estimation algorithm based on BST and extraction of directly scattered waves (SEABED)

The associate editor coordinating the review of this manuscript and approving it for publication was Chun-Hsing Li.

[14]–[16], can achieve real-time 3-D imaging based on BST and inverse BST (IBST). However, SEABED is quite sensitive to small range errors and the image obtained by SEABED deteriorates in noisy environments since it utilizes derivatives of the received wavefront and cannot completely remove the instability. Envelope [17], [18] uses the envelope of circles to establish the correspondence. This method does not utilize derivatives of received wavefront and can realize robust imaging for arbitrary shape targets. By calculating circles with corresponding time delays for each position of the antenna and using the principle that these circles circumscribe or inscribe the target boundary, it is shown that the target shape is expressed as a boundary of a union and an intersection set of the circles. Although Envelope can recover simple-shaped targets, it requires precise connections for observed ranges to maintain the imaging quality. For complex-shaped targets or multiple targets, such connections become difficult because each antenna receives multiple echoes from multiple scattering points on the target surface, and for a complex surface, such connections are often difficult because each antenna observes multiple echoes and there are too many candidate connections. The RPM algorithm [19] uses the signal amplitude to provide an accurate estimate of the direction of arrival (DOA), which achieves a direct mapping from the observation range to the target points, eliminates the distance connection process and remarkably enhances accuracy even in complex boundary extraction. However, it still suffers from image distortion caused by multiple interfering signals with different waveforms in cases where the variation scale is smaller than a pulse-width when more complex shapes with many concave and convex structures exist.

Traditional shape reconstruction algorithms based on BST tend to treat all reflections as single reflection, while for complex targets, especially concave targets, there are often multiple reflections within them, and some parts of the target are only visible by multiple reflection echoes rather than single reflection, which will lead to the partial absence of the reconstructed target shape. Multiple reflections from complex targets have been studied in the fields of RCS measurements, SAR imaging, and electromagnetic (EM) inverse scattering [20]–[22], but in general there is a lack of research on the mechanism of the effect of multiple reflections on shape reconstruction. [23] exploits two reflections for target reconstruction, which extends the visible range of the target, but still fails to provide a complete reconstruction of the concave target because it does not utilize all the high-order reflection information. [24] chooses a typical near-field monostatic cylindrical imaging scenario with dihedral structures for discussion, investigates the mechanism of multiple reflections and the causes of artifacts in traditional methods, establishes a forward model containing multiple reflections using the shooting and bouncing rays (SBRs) method [25]–[28], and proposes a new image reconstruction algorithm. The algorithm has also been effectively extended to the multi-station cases [29], [30]. The algorithm can effectively eliminate the artifacts in traditional imaging algorithms and enables accurate imaging of complex targets. However, similar to traditional image reconstruction algorithms, these algorithms also suffer from low computational efficiency and slow imaging speed.

In this paper, we propose a shape reconstruction algorithm based on high-order boundary scattering transform (HBST). Unlike the monostatic linear scanning geometry adapted in the conventional BST algorithm, we choose a near-field monostatic cylindrical scanning scenario with dihedral structures for discussion. Furthermore, we analyze the causes of artifacts and propose a forward model between the dihedral target's shape and the time-domain wavefront by analyzing the path propagation mechanism of electromagnetic waves within the concave structure with the SBR method. Then the shape reconstruction algorithm which processes each reflection signal separately is derived. The algorithm effectively eliminates artifacts appearing in the conventional BST algorithm and improves the reconstruction accuracy. Both simulation and experimental results prove the effectiveness of the algorithm for dihedral-like structures.

The rest of the paper is organized as follows. Section II analyzes the causes of artifacts in dihedral structures using the ray-tracing method. In Section III, we derive the forward model based on the research of propagation path of odd reflections and put forward a novel shape reconstruction algorithm which connects the received time-domain wavefront with the target shape and eliminates target artifacts effectively. Numerical simulations and experimental results are presented in Section IV. Section V summarizes the results and is the conclusion of this paper.

II. ARTIFACT ANALYSIS

Multiple reflections within concave structures are always treated as single reflection based on the Born approximation [31] in conventional imaging algorithms, and artifacts often appear in such cases. To investigate the relationship between multiple reflections and imaging artifacts, we choose dihedral within which multiple reflections generally exist as typical concave structure for analysis, as shown in Figure 1(a). Here we adapt a monostatic cylindrical scanning scenario and represent the target dihedral's position (r, θ) in polar coordinates. We define the opening angle as 2φ (from the left edge $\theta = +\varphi$ to the right edge $\theta = -\varphi$), the angle in which the angle bisector of the dihedral locates as $0°$, and the vertex of the dihedral locates at the scanning center $(0, 0)$. Note that when the vertex of the target dihedral is not at the scanning center $(0, 0)$, we can still transform it to be equivalent to the case where the vertex is at the center by a coordinate transformation operation, which will be mentioned later. In our simulation, the target dihedral with a $40°$ opening angle ($\varphi = 20°$) has edge length L of 0.3 m, scanning angle θ_{sca} of the multi-monostatic transceiver varing from $-60°$ to $60°$ with $0.5°$ interval, and the scanning radius R is 0.7 m. The SBRs method is utilized

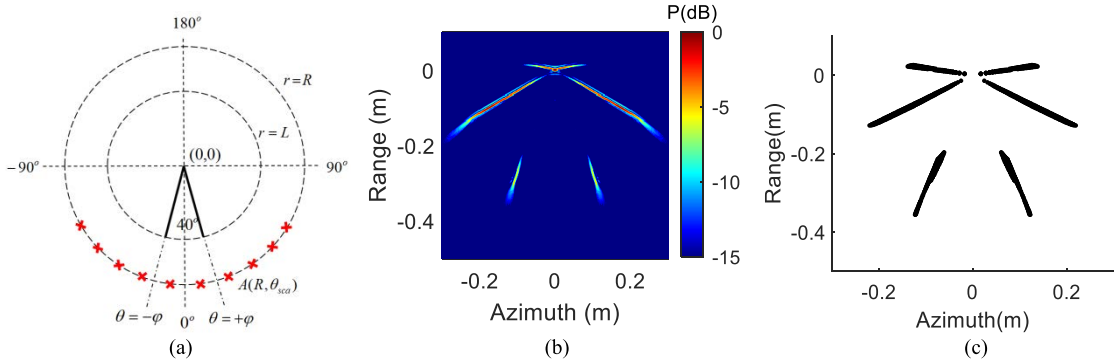

FIGURE 1. Schematic of monostatic cylindrical scanning geometry and reconstruction results of 40° dihedral structure using BP algorithm and conventional BST algorithm. (a) Cylindrical scanning geometry. (b) Reconstruction from BP algorithm. (c) Reconstruction from conventional BST algorithm.

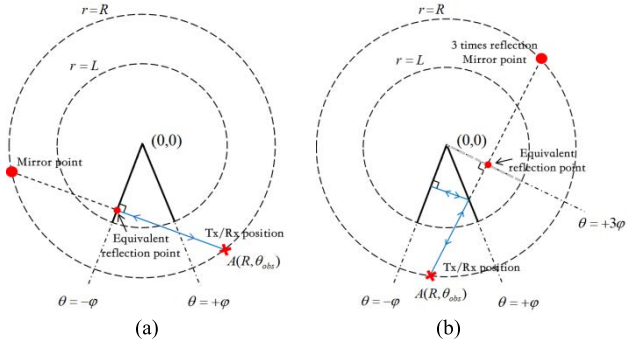

FIGURE 2. Illustration of the equivalent reflection point in the case of (a) without and (b) with multiple reflections, and the mirror reflection method is used to analyze the cause of artifacts by determining the location of the equivalent reflection point. (a) Single reflection scene (reconstruction results in no artifacts). (b) Three reflections scene (reconstruction results in artifacts).

to analyze the cause of artifacts and the received echoes are simulated in EM high-frequency approximation SBR+ algorithm from 2 to 40 GHz in electromagnetic simulation software Ansys HFSS. Since it has been shown in [24] that even reflections cannot reconstruct the target edge's length correctly, in this paper we use circularly polarized transceivers to filter out even reflections [32] and only use odd reflections for target reconstruction.

We process the received echoes from the target dihedral using the BP imaging algorithm and conventional BST algorithm respectively, and the imaging results are shown in Figure 1(b)-(c). It is obvious that both algorithms can only recover the outer edges of the dihedral while they do not effectively reconstruct the inner edges. In addition, the imaging results show the presence of artifacts corresponding to wrong dihedral shape with larger angles. In the following discussion, we use the abbreviation RT to denote the number of reflection times, for example, mRT represents the m reflection signal.

We assume that the metallic dihedral structure is electrically large target and satisfies the high-frequency approximation condition, then the electromagnetic wave can be regarded as ray satisfying the mirror reflection principle, which simplifies the analysis of the propagation path by determining consecutive mirror points of dihedral edges. Since both algorithms treat all reflected signals as 1RT signal, we can analyze the causes of artifacts by determining the position of the equivalent reflection points of different RTs. If all RTs within the dihedral are considered as 1RT, the position of the equivalent reflection points of each RT is where the reconstructed target locates. For 1RT, as shown in Figure 2(a), the equivalent reflection point locates on the edge of the dihedral, so the outer edge of the dihedral can be recovered correctly according to the 1RT echo. However, for multiple reflection echoes, such as 3RT in Figure 2(b), the equivalent reflection point locates outside of the dihedral, and if multiple reflection echoes are processed as 1RT, the dihedral artifact will appear. According to the mirror reflection principle, it can be proved that in this case the opening angle of the artifact is 3 times as large as the real angle, i.e., $3 \cdot 2\varphi$. Similarly, for any high-order odd reflection signal (mRT, m = odd, $m > 1$), if it is treated as 1RT, artifact with an opening angle of $m \cdot 2\varphi$ will appear. There are 1,3,5RT signals within the 40° dihedral, since they are all treated as 1RT in both algorithms, artifacts with opening angle of 120° and 200° appear, as shown in Figure 1(b)-(c).

III. HIGH-ORDER BOUNDRARY SCATTERING TRANSFORM (HBST)

Treating high-order reflections as single one can cause imaging artifacts, so in the following discussion we will analyze the propagation law of each reflection and process them separately. Meanwhile, by establishing the correspondence between the received wavefront and the target shape, we can reconstruct the shape of the dihedral structure with the wavefront directly, which significantly reduces calculation and saves processing time. We firstly analyze the propagation path of odd reflections and build a forward model from the dihedral shape to the time-domain wavefront, and summarize the distribution of each reflection in the wavefront. Then, we derive a high-order reconstruction algorithm considering multiple reflections for recovering the shape of the target from the received wavefront.

TABLE 1. Common opening angles and corresponding maximum number of reflection times (MRT).

Opening angle (°)	**180**	150	**90**	70	**60**	55	**45**	40	**36**
MRT	**1**	2	**2**	3	**3**	4	**4**	5	**5**

A. HIGH-ORDER FORWARD MODEL

The number of reflection times of the echoes within the concave structure is related to its opening angle. From [24], we can conclude that the relationship between the maximum number of reflection times (MRT) and the opening angle 2φ of the dihedral in the cylindrical scanning is

$$\mathrm{MRT} = \mathrm{ceil}\left(180^\circ/2\varphi\right) \tag{1}$$

where ceil indicates upward rounding. Table 1 shows the relationship between common opening angles and MRT, where the bolded contents correspond to the critical angles which indicate the upcoming appearance of new higher reflections when the opening angle continues decreasing. It is obvious that the MRT in the concave structure increases as the opening angle becomes small.

In the monostatic cylindrical scanning, the echo signal cannot be received at all scanning angles θ_{sca}, and the propagation distance of echoes received at different angles is not the same. The relationship between the observation angle θ_{obs} of odd reflection signals and their corresponding propagation distance R_{AB} is given in [24]

$$R_{AB} = 2Rsin\left(\left|(-1)^{inc}(2n-1)\,\varphi - \theta_{obs}\right|\right), \quad n = 1, \ldots, n_{max} \tag{2}$$

where inc $= 0$ or 1 when the rays firstly incident to the right or left side of the dihedral, respectively. R is the scanning radius, θ_{obs} is the observation angle where echoes can be received within the scanning angle θ_{sca}, $2n-1$ correspond to the number of odd reflections, and the maximum number of odd reflections is $2n_{max}-1$. n_{max} can be obtained from

$$n_{max} = ceil\,(MRT/2) \tag{3}$$

To deduce the range of the observation angle θ_{obs} for each reflection signal, we should firstly analyze the propagation path of each reflection signal. Based on the SBRs method, we have proven that there is only one case of the propagation path within the dihedral for odd RTs, i.e., the ray is eventually incident perpendicular to the edges of the dihedral and returns along the original incidence path. Figure 2(a), 18 and 19(a) show the propagation paths of the 1RT, 3RT and 5RT echoes within the dihedral, respectively. Meanwhile, it can be proved that the propagation path of even RTs does not follow the mirror reflection principle in the SBRs method, and it may be caused by the multiple coupling effect. The derivation process is described in detail in Appendix A. According to the propagation law of odd RTs within the dihedral, we can derive the range of the observation angle θ_{obs}, as shown in (4)-(6), as shown at the bottom of the page, where θ_1 and θ_2 are the boundary values of the observation angle range. Details are described in Appendix B. For any $(2n-1)$ RT signal, the observation angle ranges in the two cases, firstly incident to the right and left side of the dihedral, are symmetric about 0°, as shown in (4).

According to R_{AB} in (2) and the range of the observation angle θ_{obs} in (4), we can obtain the forward model describing the relationship between target shape and time-domain wavefront. Figure 3 shows the received time-domain signal from the dihedral structures with edge length of 0.3 m, scanning radius of 0.7 m, opening angles of 180°, 150°, 90°, 70°, 60°, 55°, 45° and 40° respectively. The time-domain signal $\mathrm{P(R_{AB}, \theta_{obs})}$ is obtained by performing an IFFT in the frequency direction on the two-dimensional signal power $\mathrm{P(f,}\theta_{obs}\mathrm{)}$ received at different frequencies and angles, and it indicates the propagation distance of strong echoes at corresponding observation angles, and the propagation distance corresponds to the time delay t with the relationship of $R_{AB} = ct/2$ (c is the speed of light). Stronger received signal power indicates stronger echo at corresponding observation angle and propagation distance. In this paper we uniformly use the normalized power. It should be noted that since we use cross-polarization in the simulation, only odd reflections are received, and the even reflections are filtered out. In Figure 3, the black solid curve which coincides with the wavefront in the time-domain signal corresponds to R_{AB} determined by (2) and (4), and it means the derived theoretical value is consistent with the actual simulation results, thus proving the correctness of the forward model. The dashed lines are obtained by substituting $\theta_{obs} = \theta_{sca}$ into (2), where the yellow and white dashed lines correspond to the echo signals first incident to the right and left sides of the dihedral, respectively.

$$\theta_{obs} \in \begin{cases} (\theta_1, \theta_2), & \textit{right edge firstly irradated} \\ (-\theta_2, -\theta_1,), & \textit{left edge firstly irradated} \end{cases} \tag{4}$$

$$\theta_1 \in \begin{cases} (2n-1)\,\varphi - 90^\circ + arcsin\left[\dfrac{L}{R}\cos(2n\varphi)\right], & 2n\varphi < 90^\circ \\ (2n-1)\,\varphi - 90^\circ, & 2n\varphi \geq 90^\circ \end{cases} \tag{5}$$

$$\theta_2 = \varphi - \arccos\left(\frac{Lcos^2\left[2\,(n-1)\,\varphi\right] + sin\left[2\,(n-1)\,\varphi\right]\cdot\sqrt{R^2 - L^2cos^2\left[2\,(n-1)\,\varphi\right]}}{R}\right) \tag{6}$$

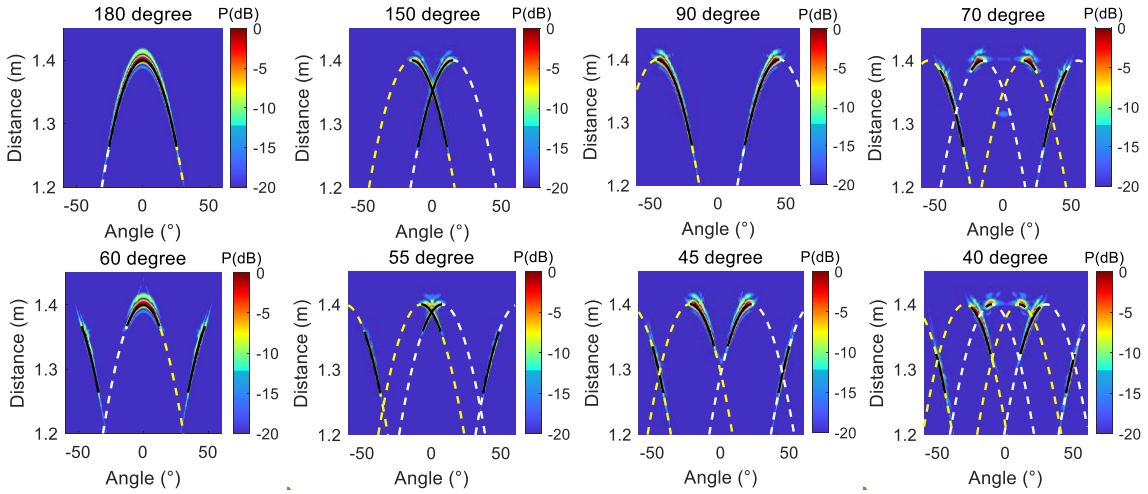

FIGURE 3. Time-domain signal of dihedrals with different opening angles (180°, 150°, 90°, 70°, 60°, 55°, 45° and 40°). Among them, the black solid curves correspond to R_{AB} determined by (2) and (4), and the dashed lines correspond to R_{AB} when $\theta_{obs} = \theta_{sca}$ in (2).

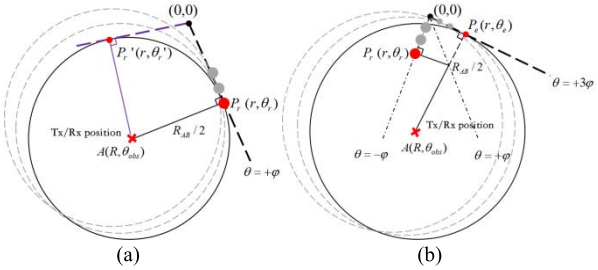

FIGURE 4. Schematic diagram of determining the vertical reflection points within the dihedral. (a) 1RT signal. (b) 3RT signal.

We can summarize the characteristics of the time-domain wavefront of dihedrals as follows. First of all, the wavefront of the signal firstly incident to the right and left edges is symmetric at 0° due to the symmetry of the dihedral. For the right-side incident signal, the slope of the its wavefront is negative because the corresponding propagation distance becomes progressively shorter during the counterclockwise circular scanning. In contrast, the slope for the left-side incident signal is positive. Second, the lower the number of reflections, the larger the corresponding observation angle θ_{obs} (the further away from 0°). As the opening angle decreases and reaches the critical angle of odd RT (e.g., 90°, 45°), higher odd RT signal appears. The observation angle θ_{obs} of the newly emerged highest odd RT signal first approaches 0° and gradually moves away from 0° in the opposite direction as the opening angle continues decreasing. In this process the wavefront corresponding to the firstly right and left incident rays go through a process of intersection and separation.

B. HIGH-ORDER RECONSTRUCTION ALGORITHM

Since the vertex of our target dihedral is at the cylindrical scanning center $(0, 0)$, and the propagation path of the electromagnetic wave within the dihedral is that the wave returns along the original path after the final vertical incidence on the edge of the dihedral. Based on this, as long as we determine the location of the reflection points, the set of all reflection points constitutes the reconstruction target. For the 1RT signal, as shown in Figure 4(a), the tangent point of the thick dashed line across the scanning center $(0, 0)$ on the circle with the antenna position $A(R,\theta_{obs})$ as the center and the one-way propagation distance $R_{AB}/2$ as the radius is the vertical reflection point of the echo on the dihedral edge, which is also our target reconstruction point. Note that there are two tangent points P_r and P_r' for each case, but unlike P_r which has the invariant angle θ_r for different propagation distances R_{AB} and observation angle θ_{obs}, the angle θ_r' of P_r' varies. Since the angle of the dihedral edge is constant, the tangent point P_r' should be discarded. For the higher reflection signal (here 3RT is used as an example, as shown in Figure 4(b)), the tangent point we obtain in the same way mentioned above is the equivalent reflection point P_e of the real reflection point P_r, as well as the fake reconstruction point when the high-order signal is processed as 1RT signal. Since the two points P_e and P_r are mirror symmetric about the first reflection edge $\theta = +\varphi$, we can determine the position of P_r from P_e. Therefore, we can calculate the position of the corresponding reflection point based on the propagation distance R_{AB} of the echoes received at different observation angles, and different RTs should be processed differently. According to this, we can establish a one-to-one correspondence between (R_{AB},θ_{obs}) and (r_t, θ_t), as shown in (7)-(9) (see Appendix C for details).

$$\psi = \arcsin\left(\frac{R_{AB}/2}{R}\right) \tag{7}$$

$$\theta_t = (-1)^{t+1}\frac{\theta_{obs} + (-1)^{inc}\psi}{2n-1} \tag{8}$$

$$\mathrm{r}_t = \frac{\sqrt{R^2 - (R_{AB}/2)^2}}{\cos[2(n-t)\theta_t]} \tag{9}$$

TABLE 2. Defined variables and their corresponding meanings.

Variables	Corresponding meanings
φ	The absolute value of the angle where the edge of the dihedral locates
θ_{obs}	Observation angle where echoes can be received in the cylindrical scanning
θ_{sca}	Scanning angle in the cylindrical scanning
R_{AB}	The propagation distance of the received echo
n	$2n-1$ is used to indicate the number of odd reflections
L	Edge length of the dihedral
R	Cylindrical scanning radius
inc	Used to indicate the direction of the first incidence. inc = 0 or 1 when the rays firstly incident to the right or left side of the dihedral

where (R_{AB}, θ_{obs}) is the set of extracted wavefront points from time-domain signal, and (r_t, θ_t) is the position of the $t_{th} \in [1, n]$) reflection point of the $2n-1$(n $\in [1, n_{max}]$) reflection signal in polar coordinate, which is also the position of the reconstructed target. We can calculate the angle θ_t of corresponding reconstruction point with wavefront point (R_{AB}, θ_{obs}) by (7)-(8), and then calculate the length r_t according to (9). It should be noted that smaller t means earlier reflection, for example, (r_1, θ_1) denotes the position of the reflection point where the $2n-1$ reflection ray firstly irradiates onto the dihedral. Larger t corresponds to a later reflection, and the irradiated area on the target is mainly concentrated on the inner part of the concave. When the signal firstly irradiates to the right or left edge of the dihedral, $inc = 0$ or $inc = 1$ in (8), respectively. If inc takes the opposite value, the reconstructed point obtained corresponds to the wrong tangent point P_r'. The final reconstructed target position is determined by the set of all (r_t, θ_t) which result from processing every RT signal with corresponding algorithm in (7)-(9). We list the frequently used variables and their definitions in Table 2 for a better understanding.

From (7)-(9), it can be seen that in order to perform the shape reconstruction correctly, it seems to be necessary to distinguish wavefront points (R_{AB}, θ_{obs}) in different RTs and different incident directions manually. However, assuming that the m_1RT signal within the dihedral is processed by the m_2RT algorithm, if treated with the correct direction of incidence, then the processed unilateral angle θ' is $m_1/m_2 \cdot \theta$, where θ is the true unilateral angle. When $m_1 \neq m_2$, θ' is still constant but not equal to θ. However, if the signal firstly incident to the right or left edge of the dihedral is treated as firstly incident to the left or right edge, we have angular deviation $|\theta - \theta'| = 2\psi/(2n-1)$. Since ψ is not a constant, the value of θ' is also variable. Based on this, we propose a method to avoid the manual division of wavefront belonging to different RTs and incident directions, thus automating the imaging. For the wavefront with MRT $= 2n_{max} - 1$ (only odd reflections are considered), we can process all odd reflections wavefront by each reflection algorithm (n_{max} sets in total) separately without distinguishing the incident direction, and obtain n_{max} sets of results. Then set a proper angle threshold and retain the angle range contained in all n_{max} sets of results and their corresponding points, discard the other points, and we can reconstruct the target shape based on the position (r_t, θ_t) of all retained points.

TABLE 3. Reconstructed opening angle of 60° dihedral when processing the m_1RT wavefront with m_2RT algorithm in correct incidence direction.

m_1RT processed with m_2RT algorithm	**1RT—> 1RT**	3RT—> 1RT	1RT—> 3RT	**3RT—> 3RT**
Reconstructed angle (°)	**60**	180	20	**60**

Figure 5 (a) and (b) show the point cloud reconstruction maps obtained by using the 1RT and 3RT algorithms for the received wavefront points (R_{AB}, θ_{obs}) from 60° dihedral, without distinguishing the incident direction. There are 1RT and 3RT signals within the 60° dihedral, and the constant reconstruction angles (60° and 180° in Figure 5(a), 20° and 60° in Figure 5(b)) appear when processing the wavefront points with reconstructed algorithm in correct incidence direction. Table 3 explains the angular correspondence. Meanwhile, the reconstruction points with other angles are obtained by processing with the wrong incidence direction algorithm. We process the extracted wavefront points with 1RT and 3RT algorithms and obtain two sets of results, respectively. Keep the points in angles that both results contain (the points covered by the black dashed lines in Figure 5(a)-(b)) and discard the other points, the we can obtain the final reconstruction target shape, as shown in Figure 5(c). Noted that since the BST algorithm is based on the relationship between points, we usually use point cloud map to represent the received wavefront and the shape of the reconstructed target. Unlike in the conventional BST algorithm where all points are represented in black and thus the scattering strength cannot be judged, here we use the different colors to indicate the intensity of power in corresponding areas.

When the vertex of the dihedral is not at the scanning center, we can transform it to be equivalent to the case where the vertex is at the center by coordinate transformation operation. As shown in Figure 6, the scanning center is the center point (0, 0) in the polar coordinate, the vertex position of the dihedral is (r', θ') and the transceiver is (R, θ_{obs}). If we regard the vertex position as center point (0, 0), the position of transceiver in the new coordinate is (r, θ) and satisfies [24]:

$$r = \sqrt{R^2 + r'^2 - 2Rr'\cos(\theta_{obs} - \theta')} \tag{10}$$

$$\theta = \arctan\left(\frac{Rsin\theta_{obs} - r'sin\theta'}{Rcos\theta_{obs} - r'cos\theta'}\right) \tag{11}$$

We can firstly reconstruct the target with the conventional BST algorithm, and in the reconstruction result, the two symmetrical edges with the smallest angle are the edges reconstructed from 1RT signal. Extending the two edges and the corresponding intersection point is the vertex of the dihedral structure, then we can determine the vertex

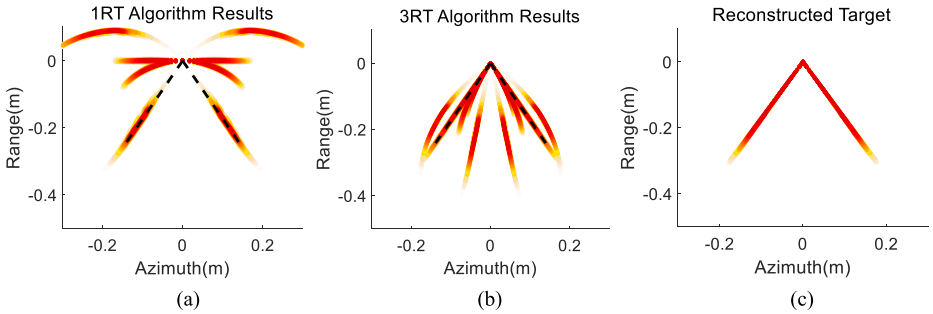

FIGURE 5. The point cloud reconstruction results obtained by processing extracted wavefront points of 60° dihedral with every odd RT algorithm separately, without distinguishing the incident direction. Reconstruction results of received wavefront points processed with (a) 1RT algorithm and (b) 3RT algorithm, (c) Final reconstruction result.

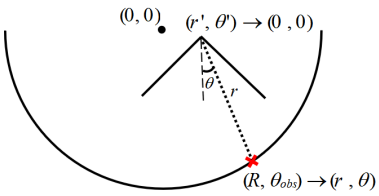

FIGURE 6. The geometry of the dihedral when the vertex is not at the scanning center.

position (r', θ'). After coordinate transformation, the observation angles θ_{obs} sampled at equal intervals under the original coordinate are converted into unevenly distributed observation angles θ under the new coordinate, and the rotation radius R, which is constant, is converted into variable r that varies with the observation angle θ. Therefore, when dealing with dihedral whose vertex are not at the center, it is firstly necessary to determine the corresponding rotation radius r and observation angle θ of each extracted wavefront point under the new coordinate by coordinate transformation operation, then reconstruct the shape according to (7)-(9).

C. ALGORITHM IMPLEMENTATION

The flowchart of the high-order reconstruction algorithm is shown in Figure 7, and Figure 8 shows the illustration of our proposed algorithm.

In our algorithm, the first step is to select a suitable power threshold and obtain wavefront points information (power value, observation angle θ_{obs} and propagation distance R_{AB}) of the strongly scattering echoes whose power is large than the threshold in the time-domain signal. Figure 8(a) shows the received time-domain signal from 60° dihedral with 0.3 m edge length, 0.7 m scanning radius. The wavefront from larger to smaller observation angles (from ±60° to 0°) belongs to 1RT and 3RT signals, respectively, and shows the propagation distance of the strongly scattering echoes at different observation angles. Figure 8(b) shows the extracted wavefront points in point cloud map, and the darker the color, the larger the corresponding power value. Noted that unlike Figure 8(a) which is an image, Figure 8(b) is a collection of reconstructed points.

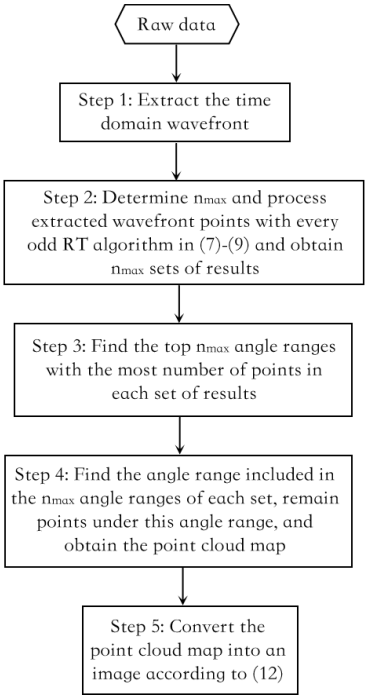

FIGURE 7. Flowchart of the proposed HBST based reconstruction algorithm.

The second step is to determine the n_{max} artificially. We firstly reconstruct the target by the conventional BST algorithm, and the smallest opening angle in the reconstructed result is the true angle 2φ of the target, then the MRT and n_{max} can be determined by (1) and (3) respectively. Then the wavefront points are processed with every $(2\mathrm{n}-1)$RT ($\mathrm{n} \in [1, \mathrm{n}_{max}]$) algorithm in (7)-(9) respectively. If the reconstruction points (r_t, θ_t) processed by the same RT algorithm without distinguishing incidence direction are considered as a set of data, then n_{max} sets of results are obtained.

There are numerous angles in each set of results. Since the angles obtained by processing with the correct incidence direction are constant, the number of points at those angles are the most. For example, the points with angles of 60° and 180° in Figure 5(a) and 20° and 60° in Figure 5(b) are the most. Noted that there is a certain deviation between the

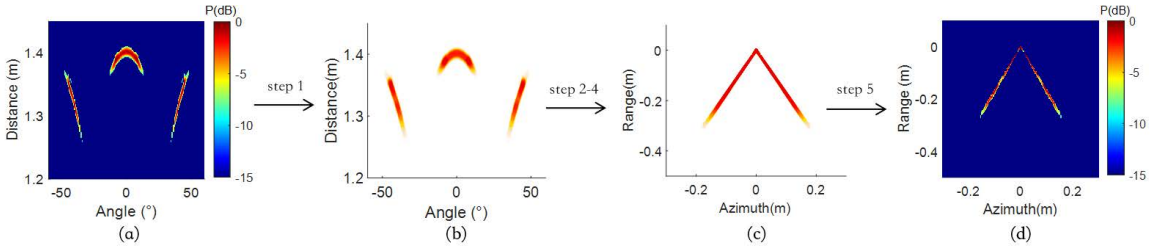

FIGURE 8. Illustration of the proposed HBST based reconstruction algorithm. (a) Received time-domain signal. (b) Extracted wavefront points in point cloud map. (c) Reconstructed target in point cloud map. (d) Reconstructed target in image.

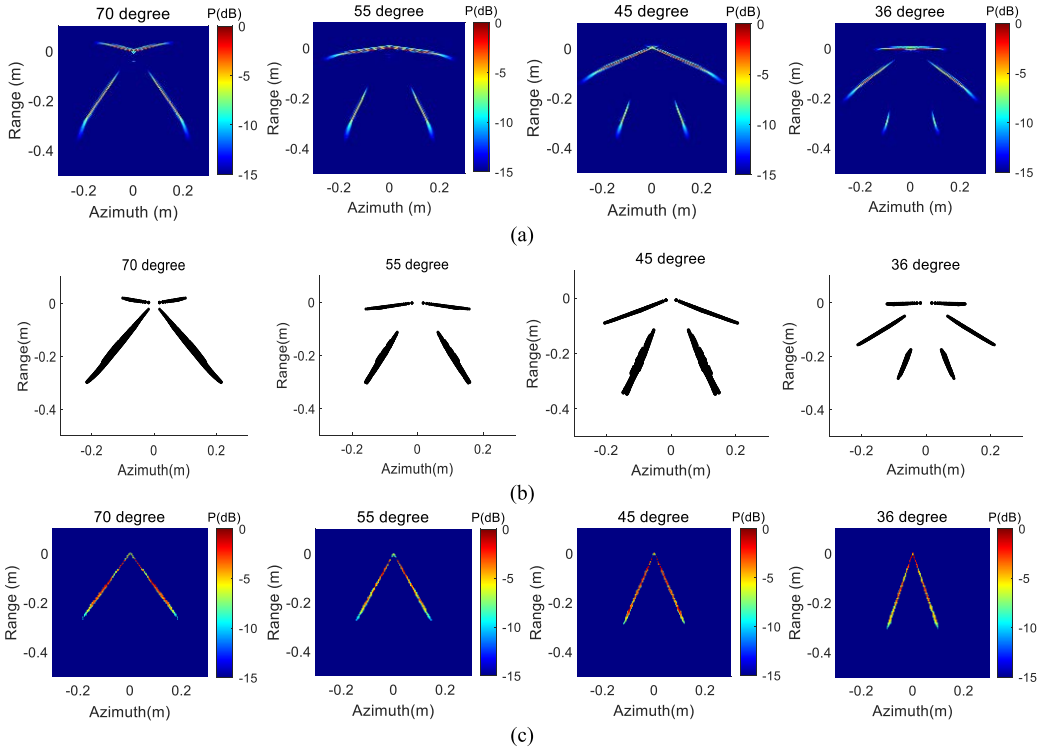

FIGURE 9. Simulation reconstruction results of dihedrals with different opening angles (70°, 55°, 45° and 36°) using (a) BP algorithm, (b) conventional BST algorithm, and (c) proposed HBST based reconstruction algorithm.

actual angle and the theoretical one when processing, so we need to set angle threshold to restrict angle range (e.g., 1°). Besides, in certain set of results, the number of reconstruction points corresponding to the correct angle is not necessarily the most, thus we cannot assume that the angle containing the most points is the target angle, and it could be any one of the n_{max} constant angles. So our next step is to find the first n_{max} angle ranges with the most points in each set of results. In this way, we can obtain $n_{max} \cdot n_{max}$ angle ranges in the n_{max} sets of results. Then calculate the mean value of each angle range for better comparison.

In the fourth step, based on the obtained $n_{max} \cdot n_{max}$ mean value of the angles, we can find the target angle that exists in all n_{max} sets of results. We can obtain the target shape in point cloud map by remaining points under the target angle and discarding the other points, as shown in Figure 8(c).

Finally, based on the information of the selected points, we can convert the point cloud map into an image by (12) to calculate the average power value P_{ij} for each pixel in the image

$$P_{ij} = \frac{\sum_{t=1}^{n} P_t}{n} \tag{12}$$

where (i, j) is the position of the pixel in the image, n is the number of reconstruction points in pixel (i, j), and P_t is the power of each reconstruction point.

IV. IMAGING RESULTS

A. NUMERICAL SIMULATION RESULTS AND ANALYSES

In the following discussion, we use the same imaging geometry and frequency as in Figure 1, and different algorithms are implemented to reconstruct the shape of dihedral with 70°, 55°, 45°, and 36° opening angles respectively. The results are shown in Figure 9 (a)-(c) using the BP algorithm, the conventional BST algorithm, and the HBST based reconstruction algorithm proposed in this paper, respectively.

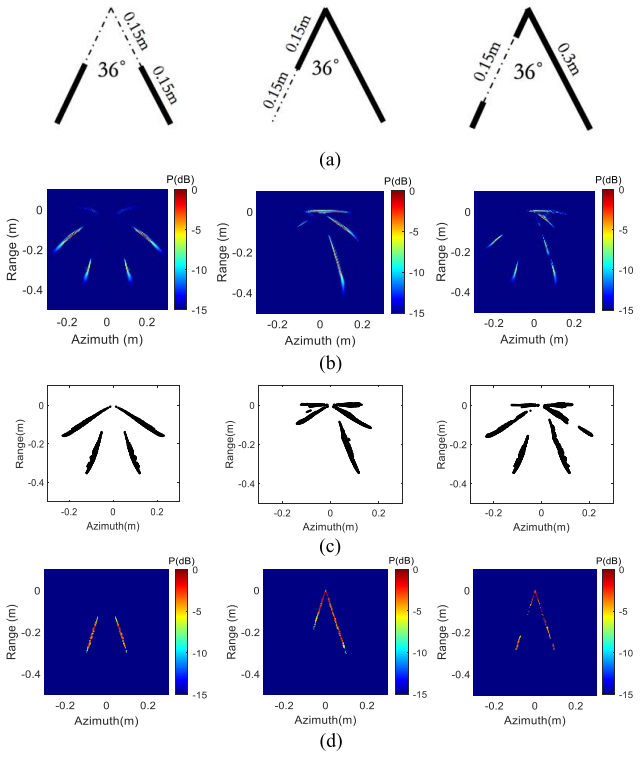

FIGURE 10. Simulation reconstruction results of dihedral with three types of notches using three different algorithms. (a) Dihedral shapes. (b) Reconstructions from BP algorithm. (c) Reconstructions from conventional BST algorithm. (d) Reconstructions from proposed HBST based reconstruction algorithm.

Since higher-order odd RTs start to appear when the opening angle is smaller than 90°, the BP algorithm and the conventional BST algorithm start to show reconstruction artifacts, and only the outer edges of the dihedral can be reconstructed correctly. For the dihedrals with 70°, 55° or 45° opening angle, 210°, 165° or 135° artifacts appear respectively because 3RT is treated as 1RT. Similarly, for the 36° dihedral, both 3RT and 5RT echoes exist. Therefore, the reconstruction results of the first two algorithms will have 108° and 180° artifacts.

It is not difficult to find that for the high-order RT echoes within the dihedral, the more times the echoes are reflected, the more regions of the dihedral can be irradiated, and the highest RT echo can irradiate all areas of the dihedral. Since the regions that are irradiated can be reconstructed, theoretically we can recover the complete dihedral only using the highest odd RT echo. For example, for a dihedral with 36° opening angle and without notches, the accurate shape can be recovered only with 5RT echo, while low-order RT echoes only can recover the outermost edge of the dihedral.

However, the highest RT signal cannot achieve the target reconstruction when faced with notched dihedral. Figure 10 shows the results of reconstructing the notched 36° dihedral with different algorithms. The edge length of the dihedral is 0.3 m, and the cylindrical scanning radius is 0.7 m. Figure 10(a) shows three types of notched dihedral

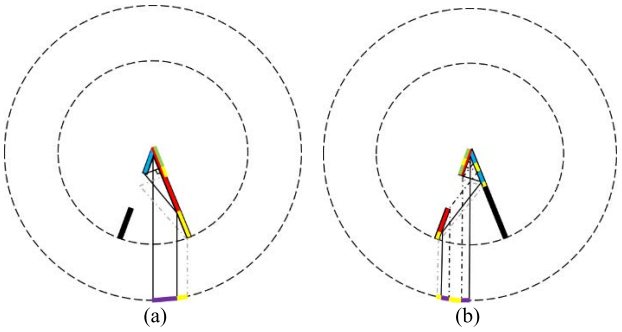

FIGURE 11. Schematic of the irradiation area of the 5RT signal which is firstly incident to the right and left edges of the notched dihedral, respectively. (a) 5RT rays are firstly incident to the right edge. (b) 5RT rays are firstly incident to the left edge.

shapes with 0.15 m edge missing from both top corners, the left outer edge, and the left middle edge, respectively. Since BP algorithm and conventional BST algorithm consider all reflections as 1RT, thus the 3RT and 5RT echoes reconstruct artifacts with opening angles of 108° and 180°, and the inner edges of the dihedral which can be recovered from higher RT signal cannot be reconstructed accurately in Figure 10(b)-(c). In contrast, the HBST based algorithm used in this paper effectively solves the artifact problem and accurately recovers the target shape, as shown in Figure 10(d).

It should be note that when the dihedral is notched, the shape cannot be recovered correctly only with the highest RT signal, and we need to superimpose the target shape reconstructed by all RTs echoes. The 5RT echo within the 36° dihedral lacking the left middle edge is illustrated here as an example. Figure 11(a) and (b) show the schematic of the irradiation area at the notched dihedral edge of the 5RT rays which are firstly incident to the right and left edges of the dihedral, respectively. The thick black line is the real outline of the dihedral, and the red, blue and green lines on the dihedral correspond to the areas which can be irradiated by the 1st, 2nd and 3rd reflections of the 5RT echo, respectively. The yellow line indicates areas which cannot be irradiated or the observation angle range where echoes cannot be received due to the presence of gap on the left edge of the dihedral, and the purple line shows the range of the observation angle where the echoes can be received. The thin black line indicates the critical situation in the propagation path of the 5RT signal, and the thin gray dashed line is the propagation path that cannot be achieved within the dihedral. It is easy to find that some areas that should have been irradiated cannot be recovered by the highest RT echo due to the presence of the dihedral gap, while these areas can still be irradiated by other lower-order odd RTs, so the exact target shape can be obtained by superimposing the reconstructed shapes of all odd RTs echoes.

In addition to reconstructing simple structures, the proposed algorithm can handle more complex targets. We performed a 360° cylindrical scanning of a complex-shaped object, and the scanning radius is 0.6 m and the rotation step is 1°. The complex-shaped object contains 60° and

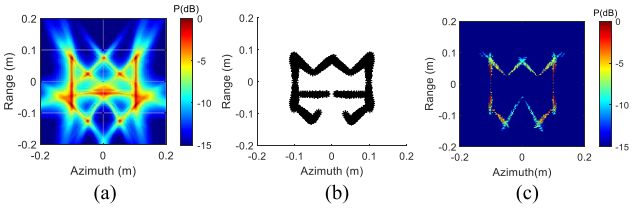

FIGURE 12. Simulation reconstruction results of complex-shaped target using (a) BP algorithm, (b) conventional BST algorithm and (c) proposed HBST based reconstruction algorithm.

TABLE 4. Comparison of accuracy and computaion time of different algorithms.

	45° dihedral		70° dihedral	
	RME	Time (s)	RME	Time (s)
BP [2]	2.08	0.46	1.55	0.48
BST [18]	1.83	0.03	1.96	0.06
[24]	0.88	32.6	0.95	32.38
HBST	0.75	0.05	0.64	0.05

90° opening angle structures, including two 90° dihedral structures with edge length of 0.07 m, a 60° dihedral structure with edge length of about 0.09 m, and two parallel edges with length of 0.15 m. Figure 12(a)-(c) show the results of reconstructing the target with the BP algorithm, the conventional BST algorithm, and our HBST based reconstruction algorithm, respectively. Since the 3RT echo within 60° dihedral is treated as 1RT echo, artifact with 180° opening angle appears in the first two methods, while our proposed algorithm effectively eliminates the artifact. It should be noted that fully automatic imaging does not work in this case, and we need to manually divide the wavefront for each dihedral structure. Meanwhile, since none of the vertex of the dihedral structures in the complex-shaped object is at the center of the cylindrical scanning geometry, a coordinate transformation operation in (10)-(11) is required when using our proposed algorithm.

In order to compare our algorithm with BP algorithm, BST algorithm and algorithm in [24] quantitatively, we imaged 45° and 70° dihedral with different algorithms and calculated the relative mean error (RME) and computation time of each imaging result, as shown in Table 4. Noted that the point cloud map of the BST algorithm is converted to image for processing.

The RME denotes the relative error of the imaging result compared to the groundtruth image, which is defined as follows [24]:

$$\mathrm{RME} = \frac{\sum_{j=1}^{N} \left| L_j^{tgt} - L_j^{gt} \right|}{\sum_{j=1}^{N} L_j^{gt}} \tag{13}$$

There are N pixel points in the imaging area, L_j^{gt} and L_j^{tgt} denote the logical value of the jth pixel point in the groundtruth image and the target image, respectively, and the value is 1 when the power value of the pixel point is

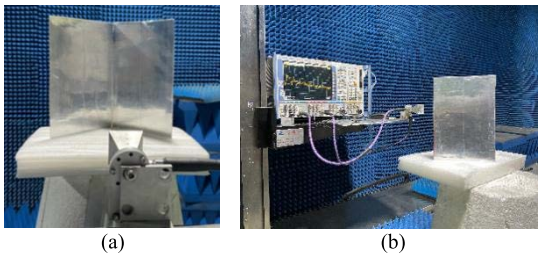

FIGURE 13. Complete dihedral with 60° opening angle and its experimental setup. (a) Front view of the 60° complete dihedral. (b) imaging scenario of the 60° complete dihedral.

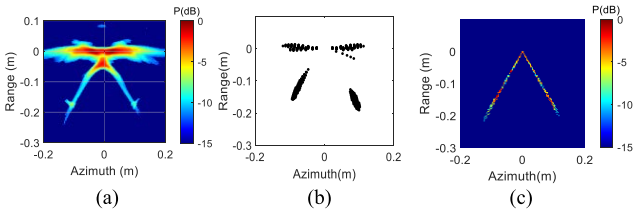

FIGURE 14. Experimental reconstruction results of the complete dihedral with 60° opening angle using (a) BP algorithm, (b) conventional BST algorithm and (c) proposed HBST based reconstruction algorithm.

greater than the threshold, and the opposite value is 0. The smaller the RME is, the more similar the target image is to the groundtruth image, i.e. the higher the accuracy of the corresponding imaging algorithm. All four algorithms are implemented with MATAB code and run on a computer with Intel i5-8300H central processing unit (CPU) @ 2.3 GHz and 24 GB random-access memory (RAM). It can be seen from Table 4 that [24] and our algorithm have higher imaging accuracy compared with BP and BST algorithm due to the consideration of multiple reflections, but [24] takes longer computation time, and our algorithm is faster due to the smaller computation based on the extracted wavefront points.

B. MEASURENENT RESULTS

The HBST based reconstruction algorithm proposed in this paper can be further verified with experimental data. We perform this near-field cylindrical scanning experiment in an anechoic chamber with a horn antenna connected to the port of vector network analyzer as transmitting and receiving antenna. Besides, a motor is connected to the turntable and controls the rotation of the mechanical turntable. A low-reflectivity foam table is placed on the turntable to hold the target to be measured. Both the motor and the vector network analyzer are controlled by the computer. In addition, the experimental frequency range is from 4 to 20 GHz with a frequency step of 0.02 GHz.

We first performed a 180° cylindrical scanning (from −90° to 90° with 1° angle step) of the 60° dihedral made of aluminum plates. In this case, the length of the measured dihedral is 0.2 m and the scanning radius is 0.6 m. Figure 13 shows the experimental scenario of the scanning on the 60° dihedral. Different algorithms are used to reconstruct the target, and the results are shown in Figure 14. Since there are 1RT and 3RT echoes reflected

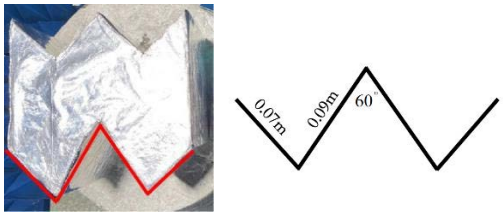

FIGURE 15. The shape of the complex-shaped target and the contour of its bottom part. (a) Top view of the complex-shaped target. (b) contour of bottom part of the complex-shaped target.

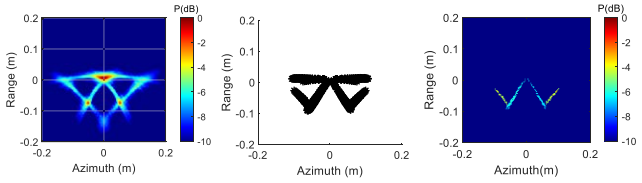

FIGURE 16. Experimental reconstruction results of the bottom part of the complex-shaped target using (a) BP algorithm, (b) conventional BST algorithm and (c) proposed HBST based reconstruction algorithm.

from the 60° dihedral, and the first two algorithms both treat 3RT as 1RT when processing, there exist artifacts with 180° opening angle for both. In contrast, the HBST based reconstruction algorithm used in this paper recovers the target shape more accurately. It should be noted that due to the slight deformation of the metallic plate during the experiment, the measured target is not a fully symmetrical 60° dihedral, so the shape reconstructed by 1RT signal has some deviation when processed using the conventional BST algorithm.

In addition, a complex-shaped target consisting of multiple dihedral structures was also tested, with the shape shown in Figure 15(a). We performed a 180° cylindrical scanning over the bottom half which is marked with red lines, and the scanning radius is about 0.7 m. The bottom half contour of the target is shown in Figure 15(b), the edge length of the middle 60° dihedral is 0.09 m, and the two outer edges are 0.07 m. The target is reconstructed using different algorithms, and the results are shown in Figure 16. The results show that for the first two algorithms which treat 3RT as 1RT, there exist 180° artifacts. Meanwhile, the reconstructed result processed by the BP algorithm has a strong reflection at the vertices of the target, and the length of the two outer edges is longer than the actual values. In contrast, the HBST based algorithm proposed in this paper reconstructs the target shape accurately.

V. CONCLUSION

In this paper, we have proposed a novel near-field millimeter-wave shape reconstruction algorithm of concave objects based on high-order boundary scattering transform. Compared with the conventional boundary scattering transform, in which all reflections are considered as a single reflection, the proposed algorithm processes high-order scattering separately in order to achieve accurate imaging of complex targets. The causes of high-order artifacts are firstly analyzed using the SBRs method. Then the forward high-order boundary scattering transform is formulated which creates the relation from target shape to time-domain wavefront. Then, the HBST-based shape reconstruction algorithm which processes wavefront corresponding to different RTs separately and recovers the target shape is further proposed. Only odd reflections are used for target reconstruction because of the ambiguity of even reflections for the recovery of target's length. Both numerical simulations and experimental results demonstrate that the proposed algorithm can efficiently recover boundaries of concave targets while eliminating high-order artifacts.

APPENDIX A HIGH-ORDER PROPAGATION PATH

To analyze each RT within the concave target, we first need to know the propagation path of each RT, and based on the propagation path we can recover the shape of the target by establishing the relationship between the time-domain wavefront and the position of the target irradiated by the rays. Here we utilize the SBRs method for the following analysis.

It is known that the angles of the left and right sides of the dihedral are $\theta = -\varphi$ and $\theta = +\varphi$ respectively, thus the opening angle of the dihedral is 2φ. For the propagation path of 1RT signal, there is only one case, that is, the ray is eventually incident perpendicular to the dihedral and then reflectsalong the incidence path, as shown in Figure 2(a). When the number of reflections is 3, the possible reflection path of the raywithin the dihedral are two types, return along the original path and return not along the original path, as shown in Figure 17(a) and Figure 18, respectively.

For the case of not returning along the original path, the angle between the reflection direction of each ray within the dihedral and the incident edge of the dihedral is acute, if $\alpha_n (n = 1, 2, 3)$ denotes the angle between the n_{th} reflection and correspondin incident edge of the dihedral, there are

$$\begin{aligned} &① \alpha_1 < 90^\circ \\ &② \alpha_2 = \alpha_1 + 2\varphi < 90^\circ \Rightarrow \alpha_1 < 90^\circ - 2\varphi \\ &③ \alpha_3 = 180^\circ - \alpha_1 - 4\varphi \\ &④ \beta = \alpha_1 - \alpha_3 > 0^\circ \Rightarrow \alpha_1 > 90^\circ - 2\varphi \end{aligned} \tag{a1}$$

It is obvious that ② is contradictory to ④ in (a1), therefore, the assumption about the propagation path of 3RT in Figure 17(a) does not work. Similarly, it can be proved that when the number of reflections is 5, the propagation path shown in Figure 17(b) is not possible. This conclusion can be applied to higher-order odd reflections. We can therefore conclude that for odd RTs within the dihedral, the only possible propagation path for rays is eventually incident vertically to the dihedral and then returns along the original incidence path, and the propagation paths of 1RT, 3RT and 5RT are shown in Figure 2(a), 18 and 19(a), respectively.

For even RTs, however, the situation is slightly different. Taking 2RT as an example, the possible reflection path of the ray within the dihedral is shown in Figure 17(c). Here we

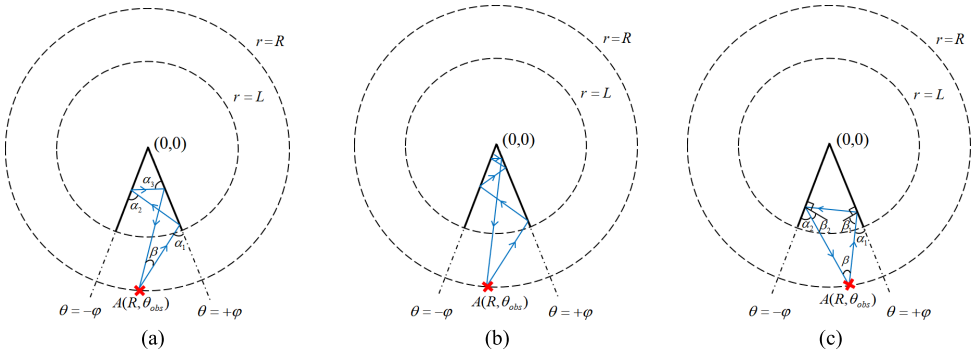

FIGURE 17. The possible reflection path of (a) 3RT, (b) 5RT and (c) 2RT echoes.

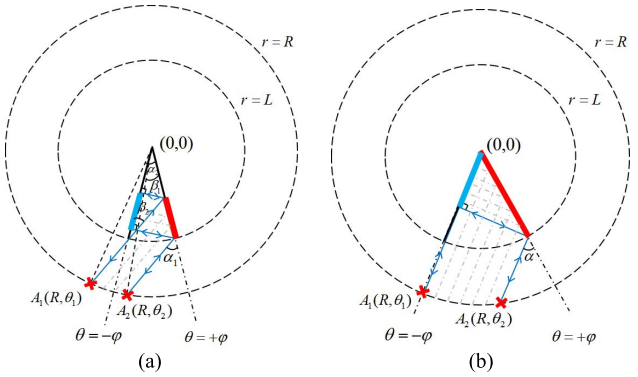

FIGURE 18. The limit case of the propagation path of 3RT signal firstly incident to the right edge of the dihedral and the areas that can be irradiated on the dihedral with different opening angles. (a) Dihedral with small opening angle. (b) Dihedral with large opening angle.

analyze the dihedral with 90° opening angle as an instance, then we have

$$\begin{aligned}
&① \ 2\varphi + \alpha_1 + \alpha_2 = 180^\circ \\
&② \ \beta_1 = 90^\circ - \alpha_1 \\
&③ \ \beta_2 = 90^\circ - \alpha_2 \\
&④ \ \beta = 180^\circ - 2(\beta_1 + \beta_2) > 0 \Rightarrow 2\varphi < 90^\circ
\end{aligned} \tag{a2}$$

Obviously, ④ in (a2) contradicts the fact that the opening angle 2φ of the dihedral is 90°, so Figure 17(c) cannot depict the propagation path of 2RT. In fact, the propagation path of 2RT does not follow the mirror reflection law, and nor do other even RTs. The even RTs are caused by the even coupling.

APPENDIX B RANGE OF OBSERVATION ANGLE

The reflected echoes are not received at all observation angles, and the number of reflections of the echoes received at different angles are different. However, according to the path propagation law of odd reflections derived in Appendix A, it is not difficult to analyze the observation angle range of each reflection in the cylindrical scanning. Figure 18(a)-(b) show all possible propagation paths of 3RT echo firstly incident to the right edge ($\theta = +\varphi$) of the dihedral and the areas that can be irradiated on the dihedral with small and large opening angles respectively, where the two thin blue solid lines are the propagation path corresponding to the critical case, and the thick red and blue line on the dihedral indicate the areas that are irradiated by the first and second reflections of 3RT, respectively. Next, we will analyze the range of the observation angle θ_{obs} of the 3RT signal as an example, and the derivation process is similar for other odd reflections.

When the opening angle of the dihedral is small, as shown in Figure 18(a), 3RT ray cannot illuminate the vertex of the dihedral, at this time there are

$$\begin{aligned}
\alpha_1 &= 90^\circ - 2\varphi \\
\beta_2 &= \alpha_1 - 2\varphi = 90^\circ - 4\varphi
\end{aligned} \tag{b1}$$

it is not difficult to find that

$$\alpha_2 = 90^\circ - 2\varphi - arcsin\left[\frac{L}{R}\sin\left(90^\circ - 4\varphi\right)\right] \tag{b2}$$

$$\beta_1 = \arccos\left(\frac{Lcos^2(2\varphi) + \sin(2\varphi)\cdot\sqrt{R^2 - L^2cos^2(2\varphi)}}{R}\right) \tag{b3}$$

Then the limits θ_1 and θ_2 of the observation angle θ_{obs} are

$$\begin{aligned}
\theta_1 &= \varphi - \alpha_2 = 3\varphi - 90^\circ \\
&\quad + arcsin\left[\frac{L}{R}\sin(90^\circ - 4\varphi)\right]
\end{aligned} \tag{b4}$$

$$\begin{aligned}
\theta_2 &= \varphi - \beta_1 \\
&= \varphi - \arccos\left(\frac{Lcos^2(2\varphi) + \sin(2\varphi)\cdot\sqrt{R^2 - L^2cos^2(2\varphi)}}{R}\right)
\end{aligned} \tag{b5}$$

Likewise, when the opening angle of the dihedral is large, as shown in Figure 18(b), 3RT can shine in all regions of the dihedral, then we have

$$\theta_1 = \varphi - \alpha = 3\varphi - 90^\circ \tag{b6}$$

In this case, θ_2 is still expressed by (b5), and by combining (b4) and (b6), it is easy to know that the critical angle of the dihedral is $2\varphi = 45^\circ$ for 3RT echo. Similarly, the range of

observation angle for other odd RTs signals can be derived, but we will not elaborate here. The conclusion is as follows (b7)–(b9), as shown at the bottom of the page.

APPENDIX C DERIVATION OF HBST BASED SHAPE RECONSTRUCTION ALGORITHM

Based on Appendix A and B, we can establish the relationship between the propagation distance R_{AB} and the observation angle θ_{obs} with the edge length r_t of the dihedral and the angle θ_t where the edges locate. The 5RT signal firstly incident to the right edge ($\theta = +\varphi$) of the 36° dihedral is used here as an example, and the derivation is similar for other cases.

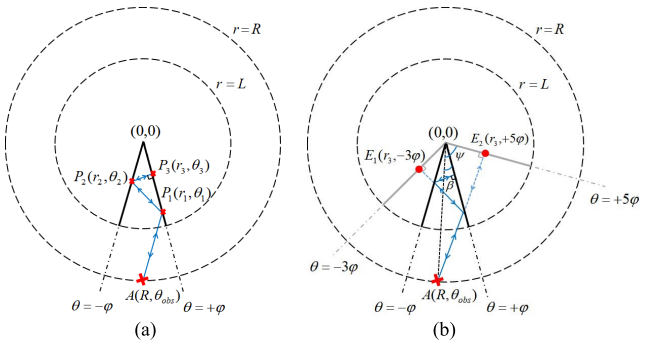

FIGURE 19. The propagation path of the 5RT signal within the dihedral. (a) Real propagation path of the 5RT signal. (b) Equivalent propagation path of the 5RT signal with mirror reflection principle.

Figure 19(a) shows the propagation path of the 5RT signal, and point $P_t(t = 1, 2, 3)$ is the reflection point on the dihedral. (r_t, θ_t) is the corresponding position of the point P_t in the polar coordinate, and based on the position we can reconstruct the shape of the dihedral. Figure 19(b) shows the equivalent propagation path of the 5RT signal according to the principle of mirror reflection, where E_1 and E_2 correspond to the 3RT and 1RT equivalent reflection points of point P_3, and the corresponding angles are -3φ and $+5\varphi$, respectively. Since the angle ψ between the observation angle θ_0 and the angle of 1RT equivalent reflection edge $\theta = +5\varphi$ is

$$\psi = \arcsin\left(\frac{R_{AB}/2}{R}\right) \tag{c1}$$

Then the angle β between the observation angle θ_{obs} and the right edg's angle $\theta = +\varphi$ of the dihedral can be obtained as

$$\beta = \psi - 4\varphi \tag{c2}$$

The observation angle θ_{obs} therefore is

$$\theta_{obs} = \varphi - \beta \tag{c3}$$

Then the angle of the right edge of the dihedral is

$$\theta = +\varphi = \theta_{obs} + \beta = \theta_{obs} + \psi - 4\varphi \tag{c4}$$

The final result by simplification is

$$\theta = +\varphi = \frac{\theta_{obs} + \psi}{5} \tag{c5}$$

The result in (c5) corresponds to the angle at which the first and third reflection points locate, while the second reflection locates at the angle

$$\theta = -\varphi = -\frac{\theta_{obs} + \psi}{5} \tag{c6}$$

Meanwhile, from Figure 19(b) it is not difficult to derive the length of the edge

$$\mathrm{r}_3 = \sqrt{R^2 - (R_{AB}/2)^2} \tag{c7}$$

$$\mathrm{r}_2 = \frac{\sqrt{R^2 - (R_{AB}/2)^2}}{\cos(2\varphi)} \tag{c8}$$

$$\mathrm{r}_1 = \frac{\sqrt{R^2 - (R_{AB}/2)^2}}{\cos(4\varphi)} \tag{c9}$$

Similarly, we can infer the case of firstly incident to the left edge and extend to higher odd RTs echoes. Then we can finally summarize the reconstruction algorithm as follows (t denotes the $t_{th} \in [1, n]$) reflection of the $2\mathrm{n} - 1(\mathrm{n} \in [1, \mathrm{n}_{max}])$ reflection signal in polar coordinate system):

$$\theta_t = (-1)^{t+1}\frac{\theta_{obs} + (-1)^{inc}\psi}{2n - 1} \tag{c10}$$

$$\mathrm{r}_t = \frac{\sqrt{R^2 - (R_{AB}/2)^2}}{\cos[2(n-t)\theta_t]} \tag{c11}$$

$$\theta_{obs} \in \begin{cases} (\theta_1, \theta_2), & \textit{right edge firstly irradated} \\ (-\theta_2, -\theta_1,), & \textit{left edge firstly irradated} \end{cases} \tag{b7}$$

$$\theta_1 \in \begin{cases} (2n-1)\,\varphi - 90^\circ + arcsin\left[\dfrac{L}{R}\cos(2n\varphi)\right], & 2n\varphi < 90^\circ \\ (2n-1)\,\varphi - 90^\circ, & 2n\varphi \geq 90^\circ \end{cases} \tag{b8}$$

$$\theta_2 = \varphi - \arccos\left(\frac{Lcos^2\left[2\,(n-1)\,\varphi\right] + sin\left[2\,(n-1)\,\varphi\right]\cdot\sqrt{R^2 - L^2cos^2\left[2\,(n-1)\,\varphi\right]}}{R}\right) \tag{b9}$$

REFERENCES

[1] D. C. Munson, J. D. O'Brien, and W. K. Jenkins, "A tomographic formulation of spotlight-mode synthetic aperture radar," *Proc. IEEE*, vol. 17, no. 8, pp. 917–925, Aug. 1983.

[2] S. Demirci, H. Cetinkaya, E. Yigit, C. Ozdemir, and A. A. Vertiy, "A study on millimeter-wave imaging of concealed objects: Application using back-projection algorithm," *Prog. Electromagn. Res.*, vol. 128, pp. 457–477, 2012.

[3] M. D. Desai and W. K. Jenkins, "Convolution backprojection image reconstruction for spotlight mode synthetic aperture radar," *IEEE Trans. Image Process.*, vol. 1, no. 4, pp. 17–505, Oct. 1992.

[4] C. Cafforio, C. Prati, and F. Rocca, "SAR data focusing using seismic migration techniques," *IEEE Trans. Aerosp. Electron. Syst.*, vol. 27, no. 2, pp. 194–207, Mar. 1991.

[5] R. Bamler, "A comparison of range-Doppler and wavenumber domain SAR focusing algorithms," *IEEE Trans. Geosci. Remote Sens.*, vol. 30, no. 4, pp. 706–713, Jul. 1992.

[6] C. Y. Chang, M. Jin, and J. C. Curlander, "Squint mode SAR processing algorithms," in *Proc. 12th Can. Symp. Remote Sens. Geosci. Remote Sens. Symp.*, Jul. 1989, pp. 1702–1706.

[7] A. M. Smith, "A new approach to range-Doppler SAR processing," *Int. J. Remote Sens.*, vol. 12, no. 2, pp. 235–251, 2007.

[8] H. Runge and R. Bamler, "A novel high precision SAR focussing algorithm based on chirp scaling," in *Proc. Int. Geosci. Remote Sens. Symp. (IGARSS)*, May 1992, pp. 372–375.

[9] R. K. Raney, H. Runge, R. Bamler, I. G. Cumming, and F. H. Wong, "Precision SAR processing using chirp scaling," *IEEE Trans. Geosci. Remote Sens.*, vol. 32, no. 4, pp. 786–799, Jul. 1994.

[10] D. A. Wikner, J. L. Fernandes, A. R. Luukanen, C. M. Rappaport, and D. M. Sheen, "Improved reconstruction and sensing techniques for personnel screening in three-dimensional cylindrical millimeter-wave portal scanning," *Proc. SPIE*, vol. 8022, pp. 34–41, May 2011.

[11] S. S. Ahmed and L.-P. Schmidt, "Illumination of humans in active millimeter-wave multistatic imaging," in *Proc. 6th Eur. Conf. Antennas Propag. (EUCAP)*, Mar. 2012, pp. 1755–1757.

[12] S. S. Ahmed, A. Schiessl, and L. P. Schmidt, "Illumination properties of multistatic planar arrays in near-field imaging applications," in *Proc. 7th Eur. Radar Conf.*, Sep. 2010, pp. 29–32.

[13] T. Sakamoto and T. Sato, "A target shape estimation algorithm for pulse radar systems based on boundary scattering transform," *IEICE Trans. Commun.*, vol. E87-B, no. 5, pp. 1357–1365, May 2004.

[14] S. A. Greenhalgh, D. R. Pant, and C. R. A. Rao, "Effect of reflector shape on seismic amplitude and phase," *Wave Motion*, vol. 16, no. 4, pp. 307–322, Dec. 1992.

[15] S. A. Greenhalgh and L. Marescot, "Modeling and migration of 2-D georadar data: A stationary phase approach," *IEEE Trans. Geosci. Remote Sens.*, vol. 44, no. 9, pp. 2421–2429, Sep. 2006.

[16] T. Sakamoto and T. Sato, "A phase compensation algorithm for high-resolution pulse radar systems," *IEICE Trans. Commun.*, vol. 87, no. 11, pp. 3314–3321, Nov. 2004.

[17] S. Kidera, T. Sakamoto, and T. Sato, "High-resolution and real-time three-dimensional imaging algorithm with envelopes of spheres for UWB radars," *IEEE Trans. Geosci. Remote Sens.*, vol. 46, no. 11, pp. 3503–3513, Nov. 2008.

[18] S. Kidera, T. Sakamoto, and T. Sato, "A robust and fast imaging algorithm with an envelope of circles for UWB pulse radars," *IEICE Trans. Commun.*, vols. 90, no. 7, pp. 1801–1809, Jul. 2007.

[19] S. Kidera, T. Sakamoto, and T. Sato, "Accurate UWB radar three-dimensional imaging algorithm for a complex boundary without range point connections," *IEEE Trans. Geosci. Remote Sens.*, vol. 48, no. 4, pp. 1993–2004, Apr. 2010.

[20] S. Shi and H. Kobayashi, "RCS calculation software for large and complex obstacles," in *Proc. Int. Conf. Electron., Commun. Control (ICECC)*, Sep. 2011, pp. 975–978.

[21] F. Cakoni, D. Colton, and P. Monk, "Qualitative methods in inverse electromagnetic scattering theory: Inverse scattering for anisotropic media," *IEEE Antennas Propag. Mag.*, vol. 59, no. 5, pp. 24–33, Oct. 2017.

[22] D. P. Xiang and M. M. Botha, "MLFMM-based, fast multiple-reflection physical optics for large-scale electromagnetic scattering analysis," *J. Comput. Phys.*, vol. 368, pp. 69–91, Sep. 2018.

[23] S. Kidera, T. Sakamoto, and T. Sato, "Extended imaging algorithm based on aperture synthesis with double-scattered waves for UWB radars," *IEEE Trans. Geosci. Remote Sens.*, vol. 49, no. 12, pp. 5128–5139, Dec. 2011.

[24] B. Liang, X. Shang, X. Zhuge, and J. Miao, "Accurate near-field millimeter-wave imaging of concave objects—A case study of dihedral structures under monostatic array configurations," *IEEE Trans. Geosci. Remote Sens.*, vol. 58, no. 5, pp. 3469–3483, May 2020.

[25] E. G. Zelnio, R. Bhalla, H. Ling, S. W. Lee, and J. A. Hughes, "Bistatic scattering center extraction using the shooting and bouncing ray technique," *Proc. SPIE*, vol. 3721, pp. 612–619, Aug. 1999.

[26] H. Ling, S.-W. Lee, and R.-C. Chou, "High-frequency RCS of open cavities with rectangular and circular cross sections," *IEEE Trans. Antennas Propag.*, vol. 37, no. 5, pp. 648–654, May 1989.

[27] H. Ling, R.-C. Chou, and S.-S. Lee, "Shooting and bouncing rays: Calculating the RCS of an arbitrarily shaped cavity," *IEEE Trans. Antennas Propag.*, vol. 37, no. 2, pp. 194–205, Feb. 1989.

[28] R. Bhalla and H. Ling, "Three-dimensional scattering center extraction using the shooting and bouncing ray technique," *IEEE Trans. Antennas Propag.*, vol. 44, no. 11, pp. 1445–1453, Nov. 1996.

[29] B. Liang, X. Shang, X. Zhuge, and J. Miao, "Accurate near-field millimeter-wave imaging of concave objects using multistatic array," *OSA Continuum*, vol. 3, no. 9, p. 2453, 2020.

[30] B. Liang, X. Shang, X. Zhuge, and J. Miao, "Bistatic cylindrical millimeter-wave imaging for accurate reconstruction of high-contrast concave objects," *Opt. Exp.*, vol. 27, no. 10, pp. 14881–14892, 2019.

[31] L. Van Hove, "Correlations in space and time and born approximation scattering in systems of interacting particles," *Phys. Rev.*, vol. 95, no. 1, pp. 249–262, Jul. 1954, doi: 10.1103/PhysRev.95.249.

[32] W. Si, X. Zhuge, Z. Pu, and J. Miao, "Accurate near-field millimeter-wave imaging of concave objects using circular polarizations," *Opt. Exp.*, vol. 29, no. 16, p. 25142, 2021.

JUNHUI YANG was born in Nanchong, China, in 1994. She received the B.S. degree in electrical engineering from the Minzu University of China, in 2016. She is currently pursuing the Ph.D. degree with the School of Electronics and Information Engineering, Beihang University, Beijing.

Her research interests include near-field imaging algorithms and millimeter-wave measurement technology.

XIAODONG ZHUGE was born in Beijing, China, in 1982. He received the M.Sc. and Ph.D. degrees *(cum laude)* from the Faculty of Electrical Engineering, Mathematics and Computer Science, Delft University of Technology, The Netherlands, in 2006 and 2010, respectively.

After graduation, he worked as a Research Scientist at FEI Electron Optics, Eindhoven, The Netherlands, until 2014. From 2014 to 2017, he was with the National Research Institute for Mathematics and Computer Science, The Netherlands, as a Researcher. He is currently an Associate Professor with Beihang University, Beijing, where he leads a research team in the field of microwave and millimeter wave sensing and systems, with a strong focus on near-field imaging and measurements. He was a recipient of the Young Engineers Prize at the 2007 European Radar Conference in Munich, Germany, and the Prestigious Veni Grant from the Netherlands Organization for Scientific Research (NWO), from 2014 to 2017. He has been a recipient of the General Program from the National Natural Science Foundation of China, since 2021.

HUI QIAO was born in Linyi, China, in 1994. She received the B.S.E.E. degree from the Changsha University of Science and Technology, Changsha, in 2017. She is currently pursuing the Ph.D. degree with the School of Electronic and Information Engineering, Beihang University, Beijing.

Her research interests include reflectarray and ultra-wideband antennas.